ADVANCED MATERIALS
www.advmat.de

A Polymerization-Assisted Grain Growth Strategy for Efficient and Stable Perovskite Solar Cells

Yepin Zhao, Pengchen Zhu, Minhuan Wang, Shu Huang, Zipeng Zhao, Shaun Tan, Tae-Hee Han, Jin-Wook Lee, Tianyi Huang, Rui Wang, Jingjing Xue, Dong Meng, Yu Huang, Jaime Marian, Jia Zhu, and Yang Yang**

Intrinsically, detrimental defects accumulating at the surface and grain boundaries limit both the performance and stability of perovskite solar cells. Small molecules and bulkier polymers with functional groups are utilized to passivate these ionic defects but usually suffer from volatility and precipitation issues, respectively. Here, starting from the addition of small monomers in the PbI_2 precursor, a polymerization-assisted grain growth strategy is introduced in the sequential deposition method. With a polymerization process triggered during the PbI_2 film annealing, the bulkier polymers formed will be adhered to the grain boundaries, retaining the previously established interactions with PbI_2. After perovskite formation, the polymers anchored on the boundaries can effectively passivate undercoordinated lead ions and reduce the defect density. As a result, a champion power conversion efficiency (PCE) of 23.0% is obtained, together with a prolonged lifetime where 85.7% and 91.8% of the initial PCE remain after 504 h continuous illumination and 2208 h shelf storage, respectively.

Y. Zhao, P. Zhu, M. Wang, S. Huang, Dr. Z. Zhao, S. Tan, Prof. T.-H. Han, Prof. J.-W. Lee, T. Huang, Dr. R. Wang, J. Xue, Dr. D. Meng, Prof. Y. Huang, Prof. J. Marian, Prof. Y. Yang
Department of Materials Science and Engineering and California Nano Systems Institute
University of California
Los Angeles, CA 90095, USA
E-mail: yangy@ucla.edu

P. Zhu, Prof. J. Zhu
National Laboratory of Solid State Microstructures
College of Engineering and Applied Sciences, and
Jiangsu Key Laboratory of Artificial Functional Materials
Nanjing University
Nanjing 210093, China
E-mail: jiazhu@nju.edu.cn

Prof. T.-H. Han
Division of Materials Science and Engineering
Hanyang University
Seoul 04763, Republic of Korea

Prof. J.-W. Lee
SKKU Advanced Institute of Nanotechnology (SAINT) and Department of Nanoengineering
Sungkyunkwan University
Suwon 16419, Republic of Korea

The ORCID identification number(s) for the author(s) of this article can be found under https://doi.org/10.1002/adma.201907769.

DOI: 10.1002/adma.201907769

In the past decade, photovoltaic (PV) devices based on organometal halide perovskites have drawn significant attention since the pioneering work of the first all-solid-state perovskite solar cell in 2012.[1–5] Perovskite materials have properties that rival those of conventional semiconductors due to their long charge carrier diffusion length,[4,6–8] high absorption coefficients,[9–11] ease of fabrication,[12] and so on. Remarkable advances through compositional modulation, crystallization control, and interface engineering have been made on improving the PV performance, promoting the power conversion efficiency (PCE) to a certified value of 25.2%.[13] Though the remarkable efficiency is comparable with traditional PV technology based on silicon (Si) or gallium arsenide (GaAs), the long-term stability against moisture, light, and heat lags behind and remains an obstacle towards commercialization.[14,15] Thus, extending the performance longevity is urgent for organometal halide perovskite solar cells at this stage.[16]

Though device encapsulation and interface engineering have been proven to be effective to improve the stability of the perovskite devices externally,[17,18] improving the inherently unstable nature of perovskite materials should still be considered as the main approach to be investigated.[19–22] Previous researches have demonstrated that the low formation energy of detrimental defects especially at the surface and grain boundaries is responsible for perovskite deterioration.[7,12,23–25] Therefore, it is expected that passivation efforts to mitigate and reduce these defects will be beneficial to improve the device longevity and efficiency simultaneously. Among all defect types, undercoordinated lead ions (Pb^{2+}) have been shown to have relatively low formation energy and is one of the common origins of trap density.[26] From previous literature, defect passivation agents with lone-pair electrons on nitrogen, oxygen, or sulfur (such as pyridine, thiophene, and urea) have been utilized to coordinate with these positively charged defects of perovskite.[27,28] However, these commonly used small molecules usually suffer from high volatility and disorderliness, which limits their practical applications in harsh environments.[29] As an alternative approach, the substitution of small molecules by polymers with similar functional groups is

promising considering their low volatility. In previous works, there have been several attempts to apply polymeric additives to perovskite solar cells.[29–38] For example, Zuo et al. demonstrated that the incorporation of poly (4-vinylpyridine) additives into the perovskite film is an effective strategy to improve both the device efficiency and the stability.[23] Bi et al. utilized poly(methyl methacrylate) as a template to control perovskite nucleation and crystal growth and fabricated solar cells with PCE up to 21.6%.[33] However, due to the relatively strong interaction between polymers and PbI_2, precipitation in perovskite precursor solution has been seen,[23,32,38] which could act as the initiating points for the crystallization of the perovskite. These will increase nuclei centers and decrease grain size consequentially, leading to the unsatisfied passivation effect.

Herein, we introduce a polymerization-assisted grain growth (PAGG) strategy to obtain efficient and stable solar cells with a perovskite composition of $FA_{1-x}MA_xPbI_3$ (Figure S1, Supporting Information). Starting from a sequentially deposited method, monomers added in the PbI_2 precursor first enables sufficient interaction between their carbonyl groups and the PbI_2. During the following PbI_2 annealing process, an in situ polymerization process is triggered, leaving the as-formed bulkier polymers adhered onto the grain boundaries with previously established interaction. When reacting with formamidinium iodide (FAI), there will be a higher energy barrier for forming the perovskite crystals due to the sufficient polymer-PbI_2 interaction, contributing to the enlarged crystal grains. In addition, carbonyl groups of polymers at the boundaries will target at the undercoordinated Pb^{2+} and efficiently reduce the trap density, contributing to an increased PCE to 23.0%. Effective passivation, together with the hydrophobic nature of the polymer selected, will largely retard degradation rate, resulting in prominent improvements of stability.

Dimethyl itaconate (DI) with C=C and C=O functional groups was chosen as the monomers due to its moderate volatility since monomers with low boiling points will rapidly volatilize before the polymerization process. The proper amount of DI was added into the PbI_2 precursor (using a mixed solvent of dimethylformamide and dimethylsulfoxide (DMSO)), along with 0.01% molar ratio of azobisisobutyronitrile (AIBN) added as the initiator, which fast decomposed at high temperature (150 °C, the annealing temperature of perovskite) and did not remain in the final perovskite films (Figure S2, Supporting Information).[39,40] Due to the lone electron pairs from the oxygen atoms of the ester groups, the DI monomers can act as a Lewis base to form an adduct with PbI_2 in the precursor, and the interaction is preserved after the spin-coating of the PbI_2 film (**Figure 1**a). During the PbI_2 annealing process, the DI monomer underwent polymerization where the C=C bonds of the monomers were cleaved and then subsequently relinked with adjacent monomers to form polymer, without sacrificing the interaction with Pb^{2+} by the C=O groups. Thus, the small DMSO molecules in the solvent could be inserted into the PbI_2 interlayers to remain the intermediate adduct, but the bulkier polymers were expelled to the grain boundaries (Figure 1a). When reacting with the organic molecule FAI, the energy barrier for the exchange of DMSO by FAI is relatively small compared to the exchange of the polymer, which is proved by the simulation in Figure 1b–d. The binding energies (defined as $E_{\text{molecule}-PbI_2} - E_{\text{molecule}} - E_{PbI_2}$) of DMSO-$PbI_2$, DI monomer-$PbI_2$, and DI dimer-$PbI_2$ are –0.83, –1.05, –1.61 eV, respectively, showing an enlarged value for DI with PbI_2 compared to DMSO. Considering the moderate binding energy of FAI and PbI_2 (–0.99 eV) (Figure S3, Supporting Information), it is more difficult for DI polymer to be exchanged from the structure by FAI.

We firstly performed Fourier-transform infrared (FTIR) spectroscopy measurements to detect the polymerization process of the DI monomers before and after the annealing process. From **Figure 2**a, the pure DI monomers exhibit the characteristic peaks of the C=O (around 1737 cm^{-1}), C=C (around 1636 cm^{-1}), and $=CH_2$ (around 898 cm^{-1}) groups,[38] which all retain in the PbI_2 film with DI. After the annealing step of PbI_2, the C=C stretch and $=CH_2$ bend both vanish, indicating a complete polymerization transformation. Compared to the control sample, the crystalline property of target PbI_2 film did not show obvious difference, with part of PbI_2 (DMSO) component remaining in the PbI_2 film (Figure S4, Supporting Information). Photographs of pure DI before and after polymerization are shown in Figure 2b,c for further confirmation, where the polymerized product visually appeared as a transparent solid-state elastomer (Figure 2c), while the DI monomers before polymerization were in a liquid state (Figure 2b). After the formation of the PbI_2 film, FAI solution in isopropyl alcohol (IPA) was spin-casted on the film to induce the intermolecular exchange to form the perovskite phase.[41] The resultant perovskite film also shows the same C=O stretch, demonstrating the preservation of the polymer after the two-step process (Figure 2a). This crystallization process is mainly related to the exchange of DMSO molecules with the FAI molecules (Figure 1a). Due to the large size of the polymerized DI and also the strong interaction with Pb^{2+}, it will be much harder for the FAI to exchange with the polymer molecules. Therefore, nuclei formation and thus perovskite crystallization occurs in regions without polymer with priority, enabling the polymers to remain unreacted at the grain boundaries. This process was confirmed with the high-resolution transmission electron microscopy (HRTEM) images of PbI_2 films after the polymerization and the as-converted perovskite films (Figure 2d,e, respectively). An amorphous area is clearly distinguishable between the contiguous grains, indicating the gathering of polymer molecules between them, which is consistent with the previous findings with polymer additives.[29,38] The thermogravimetric analysis (TGA) of pure DI polymer, perovskite and perovskite-DI polymer powder is provided in Figure S5, Supporting Information, which further confirms the existence of DI polymer. The Fast Fourier Transform (FFT) images and lattice distances for PbI_2 and perovskite grains are also shown, demonstrating a plane distance of 3.7 and 3.2 Å. They match well with the (100) reflection of the hexagonal PbI_2 phase and the (001) reflection of the cubic perovskite phase, respectively.[42,43] These immobile polymers are suitable to serve as the passivation agent along the grain boundaries by interacting with the undercoordinated Pb^{2+} without introducing more defects inside the grain interior, which is probable in some other cases for small additives.

According to the Arrhenius equation, crystallization kinetics is inversely exponentially proportional to the activation energy (E_a) at constant temperature. Due to the higher binding energy between DI monomer and PbI_2 than that between DMSO

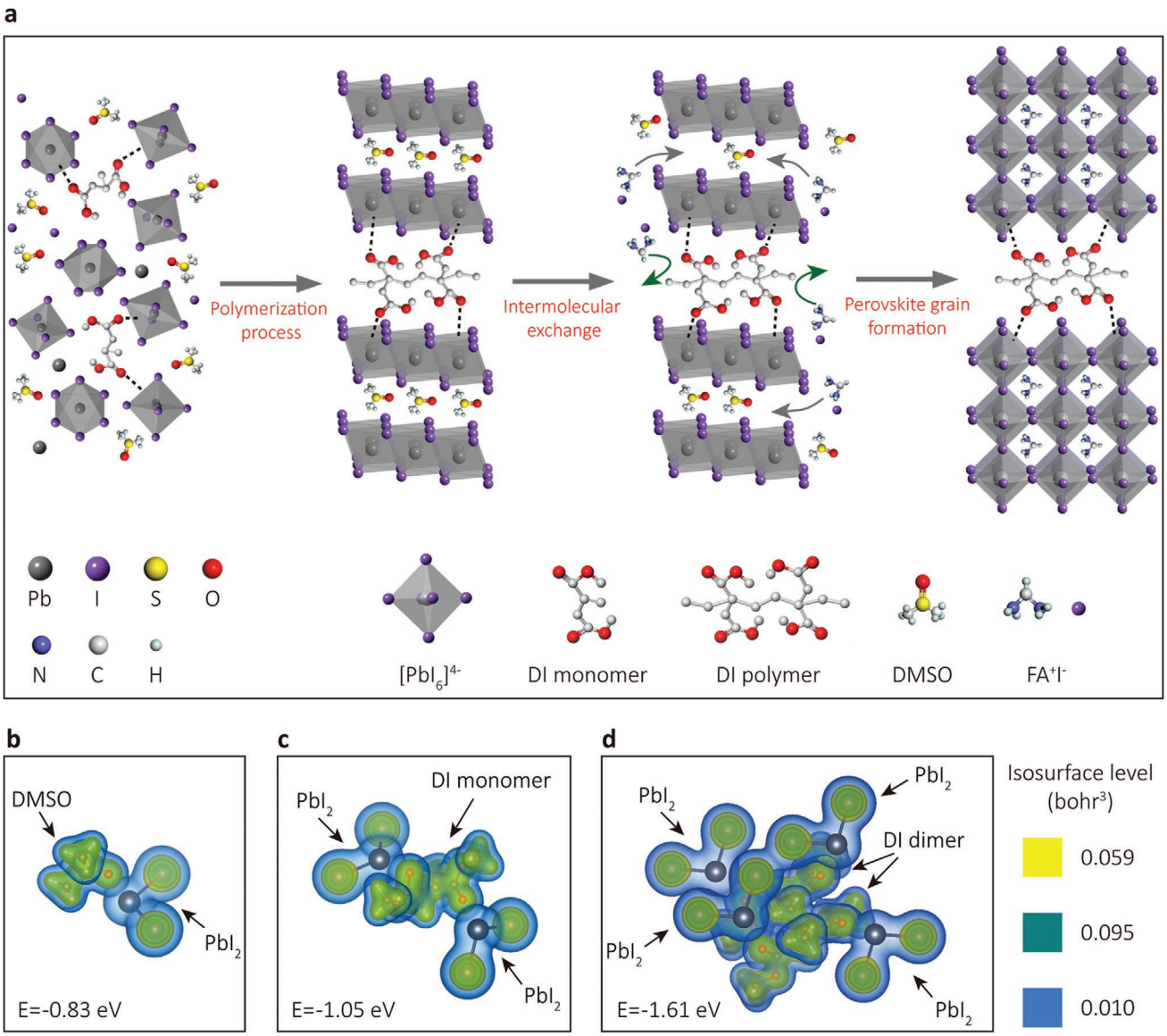

Figure 1. Illustration of polymerization-assisted grain growth (PAGG) process and the binding energies between additives and PbI_2 molecules. a) Schematic illustration of the PAGG process. b–d) Computational study of most favorable molecular configurations and binding energies between the PbI_2 molecule and DMSO (b), the PbI_2 molecules and DI monomer (c), the PbI_2 molecules and DI dimer (d).

and PbI_2, we expect a higher E_a (**Figure 3**a) after the DI addition. The increased E_a will slow down the reaction and reduce the number of nuclei. To prove this assumption, we further tracked the perovskite grain growth process in situ using confocal laser scanning fluorescence microscopy (CLSFM) measurement, starting from the pure PbI_2 or PbI_2–DI (after polymerization) films (denoted as green) to the final perovskite films (denoted as red) (Figure 3b,c). After the drop-casting of the diluted FAI/IPA solution on the as-prepared PbI_2 films, a reduced amount of nucleation sites and a retarded crystallization process were observed for our PAGG process compared to the control one, which could be explained by the increased energy barrier for the substitution of the polymer by the FAI molecules (Figure 3a). As a result, larger grains and reduced grain boundaries were obtained using the PAGG strategy, confirmed by the scanning electron microscopy (SEM) images shown in Figure 3d,e, respectively. The average grain size of the control sample is about 0.75 µm (Figure 3d) while the target one is about 1.25 µm (Figure 3e), as corroborated by the atomic force microscopy (AFM) images shown in the Figure S6, Supporting Information. The cross sectional SEM image of the target sample in Figure 3f further confirms the large size distribution, showing no grain boundaries along the charge transport direction perpendicular to the substrates. The enlarged grain sizes, together with the long-range ordering with the polymers, contributed to the better crystallinity, as proved by the X-ray diffraction (XRD) studies. The intensity of the (001) peak located at 13.9° is enhanced by 1.34-fold, indicating the improved crystallinity and orientation. The DI polymers with the C=O groups effectively passivated the defects accumulated at

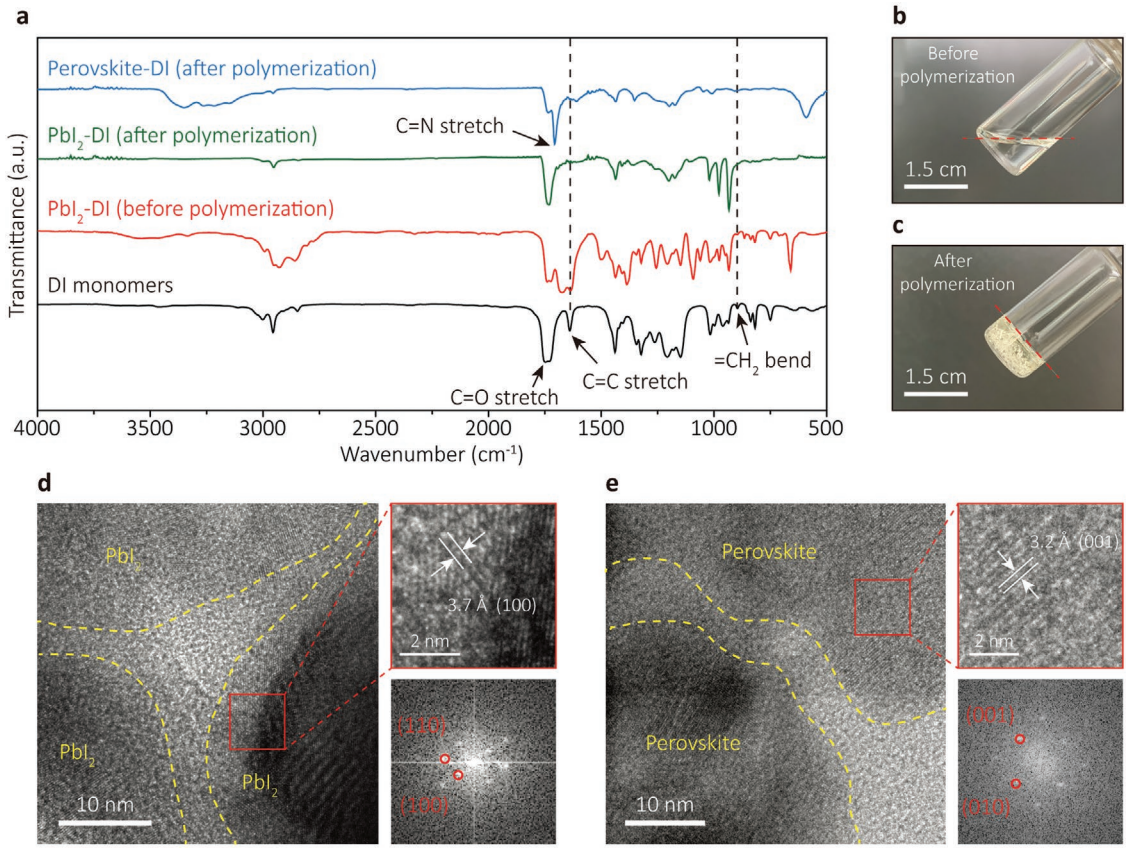

Figure 2. Confirmation of polymerization process. a) Fourier-transform infrared spectra (FTIR) of the DI monomers, PbI_2–DI film before and after the polymerization process, and perovskite film after the intermolecular exchanging process. b,c) Photographs of the pure DI monomers before (b) and after (c) the polymerization process. d,e) High-resolution transmission electron microscopy (HRTEM) images and Fast Fourier transform (FFT) analysis of the grain areas of the PbI_2–DI sample after the polymerization process (d), and perovskite sample after the intermolecular exchanging process (e).

the grain boundary regions, resulting in the better optoelectrical properties, which were investigated by photoluminescence (PL) spectroscopy. The steady-state PL shows a 1.72-fold enhancement in intensity without a noticeable shift of the peak positions (insert of Figure 3h). The time-resolved PL (TRPL) decay of the films was also measured to better compare the trap density of the films (Figure 3h). In the figure, circles indicate measured data while solid lines indicate the fitted curves with a bi-exponential decay model (detailed parameters are summarized in Table S1, Supporting Information).[29] In this model, the faster decay components are attributed to defect-assisted non-radiative recombination, while the slower decay components are assigned to bimolecular radiative recombination in the bulk.[29] The fitted parameters of the average PL lifetime is summarized in Figure 3h. The film fabricated with PAGG process demonstrated an increased fast-decay lifetime τ_1 of 130 ns, compared to that of the control perovskite film of 67 ns. Furthermore, the slow-decay lifetime τ_2 was also enhanced, from 161 ns (control film) to 370 ns (PAGG), exhibiting a longer charge carrier lifetime within the bulk crystals. The increased lifetime suggests a lower defect density of the film which mainly originates from two factors, reduced grain boundaries due to the enlarged grain sizes and efficient passivation effect by the polymer.

The photovoltaic performance of the perovskite solar cells with a device architecture of ITO/SnO_2/perovskite/spiro-OMeTAD/Ag (Figure 3f) with and without the PAGG process are compared (**Figure 4**a). With the sequentially deposited method, the control device had a short circuit current density (J_{sc}) of 24.6 mA cm^{-2}, an open-circuit voltage (V_{oc}) of 1.096 V, and a fill factor (FF) of 77.5%, which resulted in a PCE of 20.9% at reverse scan. In contrast, the addition of 1.0 mol% of the additives (Figure S7, Supporting Information) increased all the parameters to achieve a J_{sc} of 24.9 mA cm^{-2}, a V_{oc} of 1.145 V, and an FF of 80.6%. These led to an enhanced PCE to 23.0% at reverse scan. Detailed photovoltaic parameters are summarized in **Table 1**. Under continuous illumination, the stabilized PCEs tracked at maximum power point is shown in Figure S8, Supporting Information, where the target device demonstrated a steady PCE of 22.5% after 240 s, substantially superior than the 20.1% of the control. The increased V_{oc} and FF are attributed to a decreased defect density by the polymer that reduced the non-radiative recombination originating from the defects along the grain boundaries. The slight increase of J_{sc} value is due to the better charge extraction in the target devices, as indicated by the higher incident photon-to-electron conversion efficiency (IPCE) values shown in Figure 4a. The two IPCE curves display similar trends, where the integrated current densities from the IPCE spectrum are 24.4 and 24.0 mA cm^{-2}, matching with the J_{sc} values obtained from the *I*–*V* scans. We then measured the transient photovoltage (TPV) decay under the open-circuit condition to

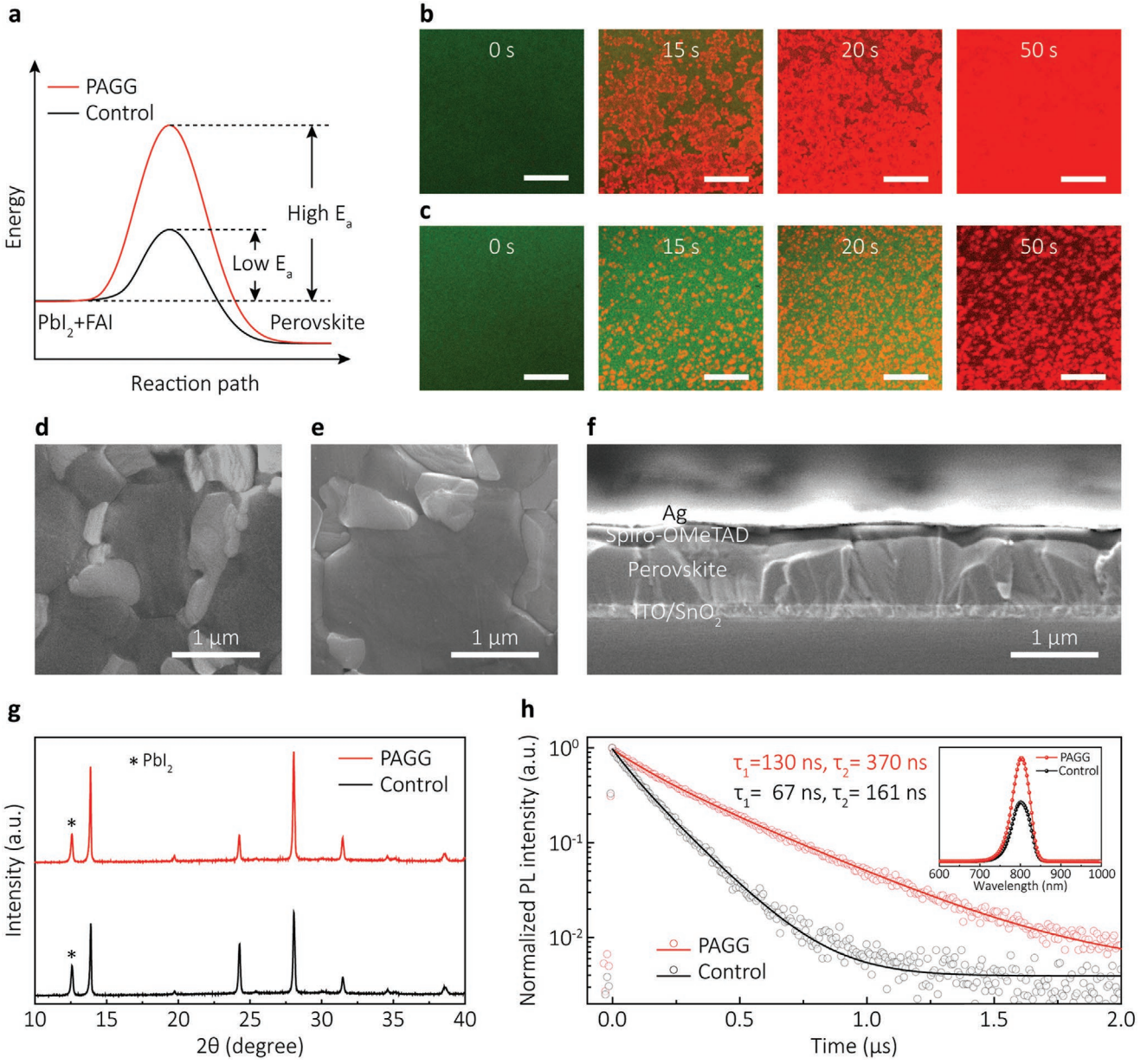

Figure 3. Intermolecular exchanging grain growth and film properties. a) Schematic diagrams of perovskite crystallization kinetics of PbI_2 films without (black) and with (red) PAGG process. b,c) Confocal laser scanning fluorescence microscopy (CLSFM) images of PbI_2 films without (b) and with (c) PAGG process as a function of time (0 s, 15 s, 20 s, 50 s) of intermolecular exchanging process. The PbI_2 regions are shown in green while the perovskite phase is shown in red in the images. Scale bars indicate 10 μm. d,e) Top-view scanning electron microscopy (SEM) images of perovskite film without (d) and with (e) PAGG process. f) Cross sectional SEM image of the solar cell device with perovskite film with PAGG process. g) X-ray diffraction spectra (XRD) of the perovskite films without (black) and with (red) PAGG process. h) Time-resolved photoluminescence (PL) spectra (Inset: steady-state PL spectra) of the perovskite films without (black) and with (red) PAGG process.

characterize the charge-recombination lifetime of the control and target devices (Figure 4c). The charge carrier lifetime of the target device is substantially longer than that of the control, consistent with the reduced non-radiative recombination from the PL results (Figure 3h). We also measured the transient photocurrent (TPC) decay under the short-circuit condition to study the charge transfer process (Figure 4d). The slightly reduced lifetime indicates a more efficient charge extraction and transfer process of our devices employing PAGG strategy.

To verify the passivation function of the resultant polymer to retard the decomposition process of the perovskite films, we used XRD to investigate the stability of the films under different harsh environments. As seen from Figure S9, Supporting Information, after 250 h storage in a 70% humidity environment, the control films obviously decomposed compared to that with PAGG process. The perovskite (001) peak to PbI_2 (100) peak intensity ratio was enhanced from 0.063 for the control film to 0.96 for the PAGG target film.

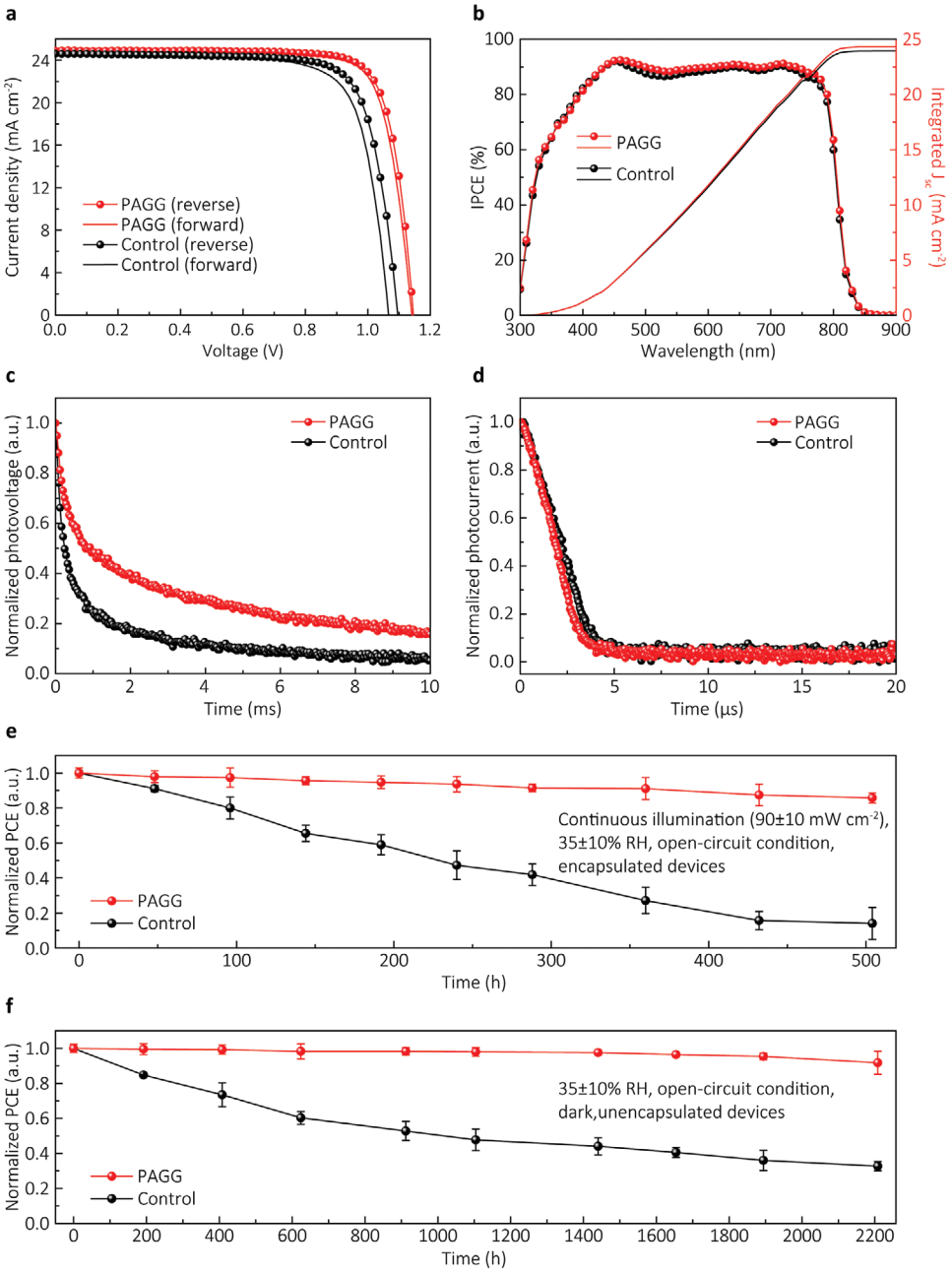

Figure 4. Improved photovoltaic performance and stability using the PAGG strategy. a) Current density–voltage (*J*–*V*) curves of perovskite solar cells without or with PAGG process. b) IPCE curves of perovskite solar cells without (black) and with (red) PAGG process. c) Transient photovoltage (TPV) decay of the perovskite solar cells without (black) and with (red) PAGG process. d) Transient photocurrent (TPC) decay of the perovskite solar cells without (black) and with (red) PAGG process. e) Evolution of the measured power conversion efficiencies (PCEs) of encapsulated perovskite solar cells without (black) and with (red) PAGG process under continuous illumination at open-circuit condition. f) Evolution of the measured power conversion efficiencies (PCEs) of unencapsulated perovskite solar cells without (black) and with (red) PAGG process exposed to ambient atmosphere at open-circuit and dark condition.

This significant difference clearly shows the stabilization effect from the PAGG process attributed to the hydrophobic nature of the formed polymer (Figure S10, Supporting Information). The thermal stability was also improved, confirmed by comparing the XRD spectra of the films heated at 85 °C in a nitrogen atmosphere for 350 h (Figure S11, Supporting Information). These various stability tests under different harsh environments demonstrate improved stability as a result of the polymerization-assisted crystallization. To quantitively confirm the stability enhancement of devices, photostability, and shelf stability of control and PAGG treated solar cells were both measured. To test the photostability of the devices, we encapsulated the devices and put them under 1-sun illumination with open-circuit condition. During the illumination, 35–40%

Table 1. Detailed photovoltaic parameters of champion perovskite solar cells with and without PAGG strategy.

Devices	Scan directions	V_{oc} [V]	J_{sc} [mA cm^{-2}]	FF [%]	PCE [%]
Control	Reverse	1.096	24.6	77.5	20.9
	Forward	1.065	24.6	75.8	19.9
PAGG	Reverse	1.145	24.9	80.8	23.0
	Forward	1.142	24.9	79.7	22.6

relative humidity and temperature of 40 °C were maintained. As shown in Figure 4e,the average PCE of the control device degraded rapidly and retained only 14.1% of its initial value. In contrast, the device treated with PAGG process retained 85.7% of its initial PCE after 504 h continuous illumination. In addition, the shelf stability of devices with PAGG process was also enhanced, maintaining 91.8% of its initial value after 2208 h storage in ambient condition without encapsulation, while only 32.6% remained in control devices. This significant difference further demonstrates the much-improved environmental stability of our devices with PAGG strategy. Since the defects on the grain boundaries and interfaces act as the major reason of perovskite material decomposition, and the former discussions clearly confirmed the efficient passivation effect of the PAGG strategy, the enhanced stability of the devices with PAGG strategy should be attributed to reduced defect density of the perovskite films.

In summary, we introduce a polymerization-assisted method to obtain perovskite solar cells improved performance and stability. By incorporating the DI monomers into the PbI_2 solution and initiating the polymerization process during the annealing step, we successfully maintained the merits of the polymer additive, and at the same time ensured sufficient adduct formation between the additive and the precursor. By utilizing the intermolecular exchange process of the two-step method, we proved that the polymer gathered at the perovskite grain boundaries, which effectively reduced the possible defects by the carbonyl groups. The enlarged grains with the lower defect density improved the PCE to 23.0% of our champion target device and achieved significantly improved photo and shelf stability. This work provides valuable insights into improving both performance and operational longevity of perovskite solar cells.

Experimental Section

Materials: Dimethylsulfoxide (DMSO, 99.7%), isopropanol (IPA, 99.7%), dimethylformamide (DMF, 99.8%), acetone (99.9%), chlorobenzene (CB, 99.8%), acetonitrile (ACN, 99.8%), 4-tert-butyl pyridine (98%), and lithium bis(trifluoromethanesulfonyl)imide (Li-TFSI, 99.95%), dimethyl itaconate (99%), and AIBN (98%) were all purchased from Sigma-Aldrich. Lead iodide beads (PbI_2, 99.999%) and SnO_2 colloidal solution (15% in water) were purchased from Alfa Aesar. Formamidine iodide (FAI) and methylammonium iodide (MAI) were purchased from GreatCell Solar (Australia). Spiro-oMeTAD (99.8%) and methylammonium chloride (MACl) were purchased from Xi'an Polymer Light Technology in China. All the materials were used without further purification.

Solar Cell Fabrication: ITO glasses were first cleaned with detergent, deionized water, acetone, and IPA for 30 min, respectively. Then, the ITO substrates were dried by the nitrogen gun and treated by UV-ozone for 20 min to remove organic residue on the surface. 0.2 mL of SnO_2 colloidal solution was diluted in 1.2 mL of deionized water and dropped on the pre-cleaned ITO glasses at a rate of 3000 rpm for 30 s, followed by annealing at 150 °C for 30 min in air. After it was cooled down to room temperature, the substrates were treated by the UV–ozone for another 10 min and transferred into the glovebox for the following steps. For the fabrication of perovskite films, a typical two-step method was employed here.1.5 M of PbI_2 in DMF and DMSO (volume ratio is 9:1) was spin-coated onto the SnO_2 films at a rate of 1500 rpm for 30 s and annealed at 90 °C for 5 min. For cross-linking samples, 1.0% molar ratio to PbI_2 dimethyl itaconate monomers were added into 1 mL of PbI_2 precursor and the spin rate remained at 1500 rpm and was also annealed at 90 °C for 5 min. Organic salts of FAI: MAI: MACl (90 mg: 6.39 mg: 9 mg in 1 mL IPA) were spin-coated on PbI_2 films at a rate of 2000 rpm for 30 s, followed with thermal annealing at 150 °C for 12 min in ambient air with a controlled humidity (30–40%). After cooled to room temperature, the perovskite films were transferred into glovebox for spiro deposition. 40 µL of spiro-oMeTAD solution, which consisted of 72.3 mg spiro-oMeTAD, 28.8 µl of 4-tert-butyl pyridine and 17.5 µL of lithium bis(trifluoromethanesulfonyl) imide (Li-TFSI) solution (520 mg Li-TSFI in 1 mL acetonitrile) in 1 ml of chlorobenzene, was spin-coated on perovskite films at a rate of 3000 rpm for 30 s. Finally, 80 nm of Ag or Au was thermally evaporated as the electrode under a high vacuum ($<3.0 \times 10^{-4}$ Pa).

Material Characterization: FTIR spectroscopy was characterized by FT/IR-6100 (Jasco) under the purge of nitrogen gas. Silicon substrates were used for FTIR measurement. The samples for FTIR measurement were prepared with the same procedure as the device fabrication but with a higher polymer content to increase the signal. TGA was conducted with SDT Q600 (TA instruments) under dry air. SEM (Nova Nano 230) and atomic force microscopy (AFM, Bruker dimension Fast Scan) with peak-force tapping mode using silicon tips (OTESPA, Bruker) were used to characterize the morphology of the perovskite films. XRD measurement was carried out by an X-ray diffractometer (PANalytical) with Cu Kα radiation at a scan rate of 3° min^{-1}. The contact angle was obtained by VCA optima 100. photoluminescence (PL) was measured by a Horiba Jobin Yvon FluoroLog-3 spectrofluorometer. A monochromatic laser with a wavelength of 640 nm was used for the excitation of perovskite films. TRPL was measured by using a Picoharp 300 stand-alone TCSPC module, and a picosecond laser diode head (PLD 800B, PicoQuant) with a wavelength of 640 nm and a frequency of 80 kHz was employed. The TPV and TPC measurements used a pulsed red dye laser (Rhodamine 6G, 590 nm) pumped by a nitrogen laser (LSI VSL-337NDS) as the perturbation source, with a pulse width of 4 ns and a repetition frequency of 10 Hz. The intensity of the perturbation laser pulse was controlled to maintain the amplitude of transient V_{oc} below 5 mV to hold the perturbation assumption of excitation light. The voltages under open circuit and currents under short circuit conditions were measured over a 1 M Ω and a 50 Ω resistor and were recorded on a Tektronix DPO 4104B digital oscilloscope. Current–voltage (*J*–*V*) characterizations of the solar cells were carried out with Keithley 2401 source meter, under simulated one sun illumination (AM 1.5G, 100 mW cm^{-2}) (Oriel Sol3A with class AAA solar simulator, Newport). The intensity calibration of the light was done by NREL-certified Si photodiode with a KG-5 filter. The solar cells were measured in an ambient atmosphere under reverse scan (+1.2 to –0.1 V) and forward scan (–0.1 to +1.2 V) with a step of 0.02 V and a delay time of 10 ms.

The EQE measurement was carried out by using a specially designed system (Enlitech) under AC mode (chopping frequency: 133 Hz) without bias light. The TEM images were taken on an FEI Titan operated at 300 kV. The PbI_2 and perovskite film was scratched off from the substrates and dispersed in IPA by sonication, which was dropped on TEM grids. To meet the high-vacuum requirement of the TEM chamber, the PbI_2 sample for TEM was annealed at 120 °C for 5 min to remove the residue of DMSO. The CLSM images were obtained by a confocal laser scanning microscope (Leica TCS SP8), using a HC PL APO oil objective (63 ×/1.40) and a 405 nm pulsed diode laser.

Computational Method: Calculations for the interaction energy as well as most stable molecular configurations were carried out by density functional theory based on first-principles calculations. The simulations were performed with the Vienna Ab initio Simulation Package (VASP) and for exchange correlation functional, the generalized gradient approximation (GGA) with the Perdew–Burke–Ernzerhof was employed to serve as pseudopotentials required for gratifyingly accurate expansion of plane-wave basis sets adopted by VASP, when frozen-core convention was realized by the projector augmented wave method.

In this work, the cut-off energy for basis sets of functions was set as 400 eV, and 1*1*1 gamma K-point were used as reciprocal point configuration. The convergence criteria of the energy differences for atomic positions relaxation were set to be 1.0×10^{-6} eV. The iso-surface of charge densities for the adducts of different combinations were visualized with the Visualization for Electronic and Structure Analysis (VESTA) software.

Supporting Information

Supporting Information is available from the Wiley Online Library or from the author.

Acknowledgements

Y.Z. and P.Z. contributed equally to this work. This work was supported by Office of Naval Research (ONR, Grant No. N00014-17-1-2484), National Science Foundation (NSF, Grant No. ECCS-EPMD-1509955), and Horizon PV. P.Z. acknowledges the China Scholarship Council (CSC) scholarship for supporting to complete the research.

Conflict of Interest

The authors declare no conflict of interest.

Keywords

defect passivation, dimethyl itaconate, intermolecular exchanging grain growth, perovskite solar cells, polymerization

Received: November 26, 2019
Revised: January 18, 2020
Published online:

[1] H.-S. Kim, C.-R. Lee, J.-H. Im, K.-B. Lee, T. Moehl, A. Marchioro, S.-J. Moon, R. Humphry-Baker, J.-H. Yum, J. E. Moser, *Sci. Rep.* **2012**, *2*, 591.
[2] M. M. Lee, J. Teuscher, T. Miyasaka, T. N. Murakami, H. J. Snaith, *Science* **2012**, *338*, 643.
[3] W. S. Yang, B.-W. Park, E. H. Jung, N. J. Jeon, Y. C. Kim, D. U. Lee, S. S. Shin, J. Seo, E. K. Kim, J. H. Noh, *Science* **2017**, *356*, 1376.
[4] S. D. Stranks, G. E. Eperon, G. Grancini, C. Menelaou, M. J. Alcocer, T. Leijtens, L. M. Herz, A. Petrozza, H. J. Snaith, *Science* **2013**, *342*, 341.
[5] N. Ahn, D.-Y. Son, I.-H. Jang, S. M. Kang, M. Choi, N.-G. Park, *J. Am. Chem. Soc.* **2015**, *137*, 8696.
[6] G. Xing, N. Mathews, S. Sun, S. S. Lim, Y. M. Lam, M. Grätzel, S. Mhaisalkar, T. C. Sum, *Science* **2013**, *342*, 344.
[7] D. Shi, V. Adinolfi, R. Comin, M. Yuan, E. Alarousu, A. Buin, Y. Chen, S. Hoogland, A. Rothenberger, K. Katsiev, *Science* **2015**, *347*, 519.
[8] Q. Dong, Y. Fang, Y. Shao, P. Mulligan, J. Qiu, L. Cao, J. Huang, *Science* **2015**, *347*, 967.
[9] Q. Lin, A. Armin, R. C. R. Nagiri, P. L. Burn, P. Meredith, *Nat. Photonics* **2015**, *9*, 106.
[10] N.-G. Park, *Mater. Today* **2015**, *18*, 65.
[11] Z. Yang, Y. Deng, X. Zhang, S. Wang, H. Chen, S. Yang, J. Khurgin, N. X. Fang, X. Zhang, R. Ma, *Adv. Mater.* **2018**, *30*, 1704333.
[12] J.-W. Lee, H.-S. Kim, N.-G. Park, *Acc. Chem. Res.* **2016**, *49*, 311.
[13] Best Research-Cell Efficiencies, https://www.nrel.gov/pv/assets/pdfs/best-research-cell-efficiencies.20190802.pdf (accessed: August 2019).
[14] Y. Yang, J. You, *Nature* **2017**, *544*, 155.
[15] H. S. Jung, N. G. Park, *Small* **2015**, *11*, 10.
[16] T. Leijtens, G. E. Eperon, N. K. Noel, S. N. Habisreutinger, A. Petrozza, H. J. Snaith, *Adv. Energy Mater.* **2015**, *5*, 1500963.
[17] Y. I. Lee, N. J. Jeon, B. J. Kim, H. Shim, T. Y. Yang, S. I. Seok, J. Seo, S. G. Im, *Adv. Energy Mater.* **2018**, *8*, 1701928.
[18] Y. Lv, P. Xu, G. Ren, F. Chen, H. Nan, R. Liu, D. Wang, X. Tan, X. Liu, H. Zhang, *ACS Appl. Mater. Interfaces* **2018**, *10*, 23928.
[19] D. W. deQuilettes, S. M. Vorpahl, S. D. Stranks, H. Nagaoka, G. E. Eperon, M. E. Ziffer, H. J. Snaith, D. S. Ginger, *Science* **2015**, *348*, 683.
[20] S. Y. Leblebici, L. Leppert, Y. Li, S. E. Reyes-Lillo, S. Wickenburg, E. Wong, J. Lee, M. Melli, D. Ziegler, D. K. Angell, *Nat. Energy* **2016**, *1*, 16093.
[21] Y. Wang, T. Wu, J. Barbaud, W. Kong, D. Cui, H. Chen, X. Yang, L. Han, *Science* **2019**, *365*, 687.
[22] Y. Wu, A. Islam, X. Yang, C. Qin, J. Liu, K. Zhang, W. Peng, L. Han, *Energy Environ. Sci.* **2014**, *7*, 2934.
[23] L. Zuo, H. Guo, D. W. deQuilettes, S. Jariwala, N. De Marco, S. Dong, R. DeBlock, D. S. Ginger, B. Dunn, M. Wang, *Sci. Adv.* **2017**, *3*, e1700106.
[24] Y. Kutes, Y. Zhou, J. L. Bosse, J. Steffes, N. P. Padture, B. D. Huey, *Nano Lett.* **2016**, *16*, 3434.
[25] J. Xue, R. Wang, K.-L. Wang, Z.-K. Wang, I. Yavuz, Y. Wang, Y. Yang, X. Gao, T. Huang, S. Nuryyeva, *J. Am. Chem. Soc.* **2019**, *141*, 13948.
[26] X. Zheng, B. Chen, J. Dai, Y. Fang, Y. Bai, Y. Lin, H. Wei, X. C. Zeng, J. Huang, *Nat. Energy* **2017**, *2*, 17102.
[27] N. K. Noel, A. Abate, S. D. Stranks, E. S. Parrott, V. M. Burlakov, A. Goriely, H. J. Snaith, *ACS Nano* **2014**, *8*, 9815.
[28] R. Wang, J. Xue, L. Meng, J.-W. Lee, Z. Zhao, P. Sun, L. Cai, T. Huang, Z. Wang, Z.-K. Wang, *Joule* **2019**, *3*, 1464.
[29] T.-H. Han, J.-W. Lee, C. Choi, S. Tan, C. Lee, Y. Zhao, Z. Dai, N. De Marco, S.-J. Lee, S.-H. Bae, *Nat. Commun.* **2019**, *10*, 520.
[30] J. Xu, A. Buin, A. H. Ip, W. Li, O. Voznyy, R. Comin, M. Yuan, S. Jeon, Z. Ning, J. J. McDowell, *Nat. Commun.* **2015**, *6*, 7081.
[31] C.-Y. Chang, C.-Y. Chu, Y.-C. Huang, C.-W. Huang, S.-Y. Chang, C.-A. Chen, C.-Y. Chao, W.-F. Su, *ACS Appl. Mater. Interfaces* **2015**, *7*, 4955.
[32] Y. Zhao, J. Wei, H. Li, Y. Yan, W. Zhou, D. Yu, Q. Zhao, *Nat. Commun.* **2016**, *7*, 10228.
[33] D. Bi, C. Yi, J. Luo, J.-D. Décoppet, F. Zhang, S. M. Zakeeruddin, X. Li, A. Hagfeldt, M. Grätzel, *Nat. Energy* **2016**, *1*, 16142.
[34] J. Jiang, Q. Wang, Z. Jin, X. Zhang, J. Lei, H. Bin, Z. G. Zhang, Y. Li, S. Liu, *Adv. Energy Mater.* **2018**, *8*, 1701757.
[35] Y. Zong, Y. Zhou, Y. Zhang, Z. Li, L. Zhang, M.-G. Ju, M. Chen, S. Pang, X. C. Zeng, N. P. Padture, *Chem* **2018**, *4*, 1404.
[36] M. Kim, S. G. Motti, R. Sorrentino, A. Petrozza, *Energy Environ. Sci.* **2018**, *11*, 2609.
[37] X. Li, M. I. Dar, C. Yi, J. Luo, M. Tschumi, S. M. Zakeeruddin, M. K. Nazeeruddin, H. Han, M. Grätzel, *Nat. Chem.* **2015**, *7*, 703.
[38] X. Li, W. Zhang, Y.-C. Wang, W. Zhang, H.-Q. Wang, J. Fang, *Nat. Commun.* **2018**, *9*, 3806.
[39] S. Guo, W. Wan, C. Chen, W. Chen, *J. Therm. Anal. Calorim.* **2013**, *113*, 1169.
[40] X.-R. Li, X.-L. Wang, H. Koseki, *J. Hazard. Mater.* **2008**, *159*, 13.
[41] W. S. Yang, J. H. Noh, N. J. Jeon, Y. C. Kim, S. Ryu, J. Seo, S. I. Seok, *Science* **2015**, *348*, 1234.
[42] M. Zhong, S. Zhang, L. Huang, J. You, Z. Wei, X. Liu, J. Li, *Nanoscale* **2017**, *9*, 3736.
[43] J.-W. Lee, Z. Dai, T.-H. Han, C. Choi, S.-Y. Chang, S.-J. Lee, N. De Marco, H. Zhao, P. Sun, Y. Huang, *Nat. Commun.* **2018**, *9*, 3021.